

Visualizing Lithium Ion Transport in Solid-State Li–S Batteries Using ^6Li Contrast Enhanced Neutron Imaging

Robert Bradbury,* Nikolay Kardjilov, Georg F. Dewald, Alessandro Tengattini, Lukas Helfen, Wolfgang G. Zeier, and Ingo Manke*

The elucidation of lithium ion transport pathways through a solid electrolyte separator is a vital step toward development of reliable, functional all-solid-state batteries. Here, advantage has been taken of the significantly higher neutron attenuation coefficient of one of the most abundant stable isotopes of lithium, ^6Li , with respect to that of naturally occurring lithium isotope mixture, to perform neutron imaging on a purpose built all-solid-state lithium–sulfur battery. Increasing the ^6Li content in the anode while using natural lithium in the solid electrolyte separator and the cathode enhances the contrast such that it is possible to differentiate, during the initial discharge, between the mobile lithium ions diffusing through the cell from the anode and those that are initially located in the solid electrolyte. The sensitivity of neutrons to the different lithium isotopes means that operando neutron radiography allows demonstration of the lithium ion diffusion through the cell while in situ neutron tomography has permitted presentation, in three dimensions, of the distribution of the trapped lithium ions inside the cell in charged and discharged states.

to large-scale energy storage.^[1–7] As variety and volume of usage have increased, the need for continuous improvement in the technologies involved has required a deeper understanding of the limitations and restrictions of the different types of Li-ion batteries. However, there are still some inherent issues with conventional Li-ion batteries, such as the flammability of the organic liquid electrolytes, which continue to offer developmental limitations. Looking at promising solutions, all solid-state batteries, with their potential for even greater energy and power densities, offer a safer alternative.^[8–12] Within this area of research, conversion-type lithium sulfur (Li–S) cells, with a high theoretical energy density of up to 2600 Wh kg^{-1} ,^[13,14] also offer the potential for significant advancement in long term stability.^[15,16] Sulfur has shown great promise as a cathode active material due to its abundance, low cost and a high

theoretical capacity of 1675 mA h g^{-1} that is much higher than the transition metal oxides employed as cathode materials in conventional Li-ion batteries.^[17] However, it is evident that performance requirements for solid-state Li–S batteries have not yet

1. Introduction

Lithium ion (Li-ion) batteries have become vital for a wide range of applications, from consumer electronics and electric vehicles

R. Bradbury, N. Kardjilov, I. Manke
Helmholtz Zentrum Berlin für Materialien und Energie
Hahn Meitner Platz 1, 14109 Berlin, Germany
E-mail: robert.bradbury@helmholtz-berlin.de;
manke@helmholtz-berlin.de

R. Bradbury
Institute for Materials Science and Technologies
Technische Universität Berlin
Strasse des 17 Juni 135, 10623 Berlin, Germany

G. F. Dewald
Institute of Physical Chemistry
Justus Liebig University Giessen
Heinrich-Buff-Ring 17, 35392 Giessen, Germany

G. F. Dewald
Center for Materials Research (LaMa)
Justus Liebig University Giessen
Heinrich-Buff-Ring 16, 35392 Giessen, Germany

A. Tengattini, L. Helfen
Institut Laue-Langevin
71 Avenue des Martyrs, 38000 Grenoble, France

A. Tengattini
University Grenoble Alpes
CNRS, Grenoble INP, 3SR
Grenoble France

W. G. Zeier
Institute of Inorganic and Analytical Chemistry
University of Münster
Correnstrasse 30, 48149 Münster, Germany

W. G. Zeier
Institut für Klimaforschung (IEK)
IEK-12: Helmholtz-Institut Münster, Forschungszentrum Jülich
48149 Münster, Germany

 The ORCID identification number(s) for the author(s) of this article can be found under <https://doi.org/10.1002/adfm.202302619>

© 2023 The Authors. Advanced Functional Materials published by Wiley-VCH GmbH. This is an open access article under the terms of the Creative Commons Attribution License, which permits use, distribution and reproduction in any medium, provided the original work is properly cited.

DOI: 10.1002/adfm.202302619

been achieved, with further improvement necessary.^[18] One important issue is the need for low impedance to the supply of ions and electrons during the electrochemical reactions while the active materials, elemental sulfur in the charged state and lithium sulfide in the discharged state, are both ionically and electronically insulating.

The performance of electrochemical cells depends on the bulk properties and microstructure of the device, both of which in turn depend on the intrinsic properties of the constituent materials. The degradation of this performance is directly related to changes to the microstructure in the electrolyte as well as the electrode materials. Additionally, in the case of solid-state Li–S cells, defects in the solid separator may impede the lithium ion transport. Consequently, it is clear that the effect of these changes during electrochemical cycling on Li⁺ ion transport pathways need to be understood.

This is especially true in solid-state batteries as the geometric resistance to Li⁺ ion transport alone is a significant limiting factor in their performance development and overall utility.^[19,20] With that in mind, several techniques have been employed that probe these structural changes in situ, including transmission electron microscopy (TEM),^[21,22] X-ray diffraction (XRD),^[23] nuclear mag-

netic resonance (NMR)^[24] and Raman spectroscopy.^[25,26] However, while these analytical methods offer insight into the structural changes in each component of the cell, they do not provide any information about the mechanism or localized effects of Li⁺ ion transport through the porous layers of the cell.

The use of 3D imaging techniques such as focused ion beam tomography (FIB), a destructive method, and X-ray micro-computed tomography (μ CT), a non-destructive method, to study the microstructure of solid-state electrodes^[27–29] and solid electrolyte (SE) interphases^[30] is well established. While both methods, either used individually or in combination, offer flexibility in image resolution and measurement time, neither are optimized for detecting the Li⁺ ions, though some work has been done using time of flight secondary ion mass spectrometry in conjunction with FIB—scanning electron microscopy for Li detection and quantification.^[31] Fortunately, techniques using neutrons have been developed that can follow the transport of Li⁺ ions within a cell under electrochemical operation. Neutron radiography has displayed its versatility with several studies quantifying lithium ion transport across cell components^[32–34] as well as visualizing structural changes to the electrolyte in situ and operando.^[35–38] The use of 3D tomography with neutrons

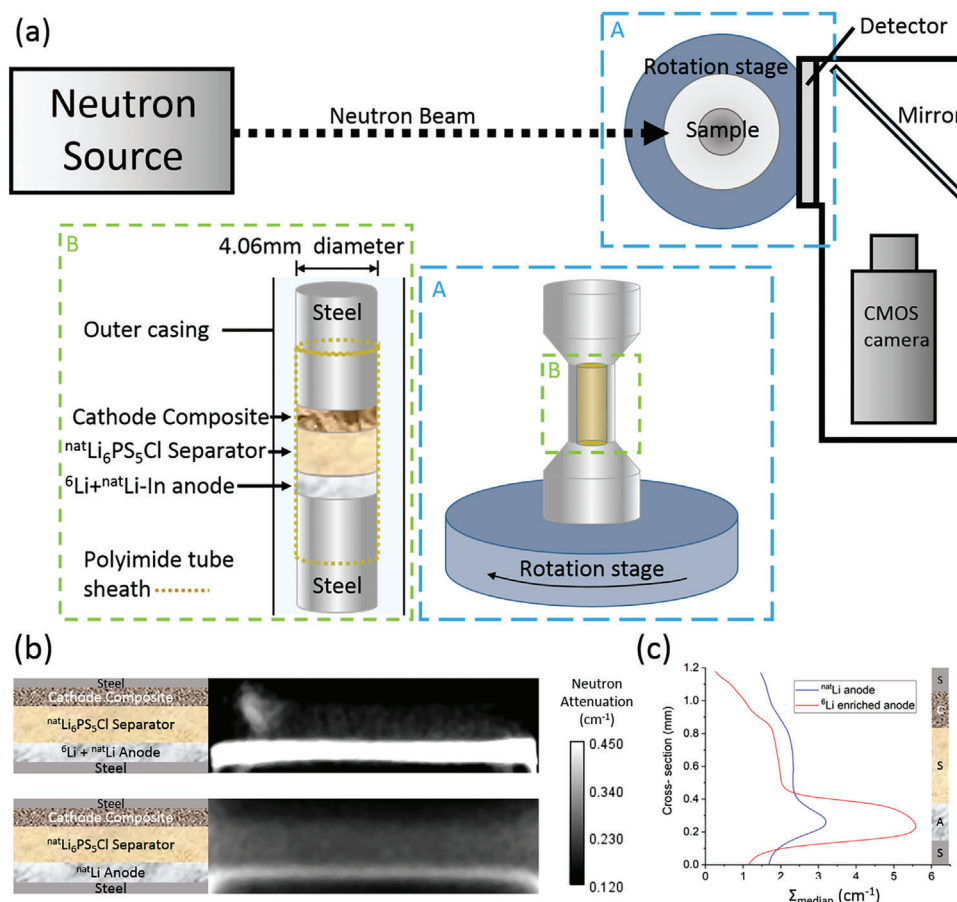


Figure 1. a) Representation of the cell setup for neutron imaging, with cell composition displayed in the expanded regions. b) Radiography images showing neutron attenuation for a cell where the Li–In anode is enriched with ⁶Li (top) and one where all Li is the naturally occurring isotopic mix (bottom). The images are displayed within the same contrast range and show a cell in the pristine state. c) Plots displaying the cross-section of the median neutron attenuation (Σ_{median}) across the images displayed in (b).

Table 1. Linear attenuation coefficients for elements, isotopes thereof, and compounds relevant to this cell. All values are for cold neutrons at a wavelength of 2.8 Å which corresponds to the maximum in the spectral distribution for a polychromatic neutron beam on the NeXT instrument.^[41]

Material	Neutron attenuation coefficient, Σ [cm ⁻¹]
^{nat} Li	5.150
⁶ Li	78.313
⁷ Li	0.067
In	11.672
^{nat} Li ₆ PS ₅ Cl	2.755
C	0.501
S	0.072
P	0.126
Cl	0.004
Al	0.112

was initially restricted to static in situ measurements due to the extended time required for collection of sufficient images to enable reconstruction of a 3D image. Additionally, limitations in image resolution restricted the dynamic changes that could be observed. However, recent increases in available neutron flux has enabled tomographies to be acquired in a much shorter timeframe, thus widening the applicability to include certain operando measurements.^[39] A neutron beam transmitted through a sample allows differentiation between elements depending on their degree of interaction with the neutron. This manifests itself in the contrast difference between those elements that are highly neutron absorbing and those that are not. In this previous study, taking advantage of the highly neutron absorbing nature of Li, 2D radiography, performed operando, revealed a Li reaction front that progressed through the cathode as the cell was cycled while in situ tomography, provided the 3D distribution of Li in the cathode at different charge states. In a cell containing Li with the naturally occurring isotopic ratio it is not possible to discern information about Li transport through the solid electrolyte separator layer due to there being no net change in the amount of Li in this region.

Here, we have attempted to visualize lithium ion transport through the solid electrolyte separator of an operando cell. In order to do this a lithium-thiophosphate-based solid-state Li–S battery (In/Li | Li₆PS₅Cl | S/C/Li₆PS₅Cl) has been used (**Figure 1a**). For this measurement though, advantage has been taken of the significant difference in neutron absorption between the two main isotopes of Li, ⁷Li and ⁶Li, which means that the naturally occurring ratio of the two isotopes (^{nat}Li), where ⁶Li ≈ 7.6% and ⁷Li ≈ 92.4% has a notably different neutron absorption coefficient to either of the isotopes in their pure form (**Table 1**). As such, anywhere that the proportion of ⁶Li is greater than ≈ 7.6% will absorb neutrons to a greater extent than the ^{nat}Li elsewhere in the cell.^[40] Additionally, in the anode, indium has an even higher neutron linear attenuation coefficient than Li (**Table 1**). This means the anode is entirely comprised of two highly neutron absorbing elements and, indeed, can be readily discerned in both images in **Figure 1b**. The lower image shows a 2D radiography image for a cell where the naturally occurring isotope mixture comprises the whole cell while the top image shows an

equivalent image for the cell used in this measurement. The degree to which the image contrast is enhanced when ⁶Li is added to the cell is clear, with brighter areas representing higher neutron attenuation, or lower transmission. In the pristine states shown in **Figure 1b**, the interface between the cathode and the separator is observable but visually indistinct due to the composition differences, namely the C and S in the cathode, that have low neutron attenuation. This results in a low image contrast between these two regions of the cell that originates entirely from the lower proportion of the Li containing solid electrolyte in the cathode compared to the pure SE separator. A plot of the neutron attenuation in cross-section across the cell axis (**Figure 1c**) shows this slight difference between the separator region and cathode composite in the initial state. Once the cell is cycled the lithium distribution changes and factors such as cell inefficiency due to trapped Li⁺ ions, in the form of Li₂S, can be studied.^[39] The difference in neutron attenuation in the separator region between the two displayed cells, both containing the same solid electrolyte is due to instrumental conditions. However, it is clear that this small variation does not account for the almost 2x increase in the total neutron attenuation, Σ , observed in the anode enriched with ⁶Li.

Thus, through enrichment of the ⁶Li content in the anode, the neutron absorption properties of the Li⁺ ions that will diffuse into the SE separator under operation have been changed with respect to the Li⁺ ions contained in the Li₆PS₅Cl SE, at least during the initial discharge. Homogenization of the Li isotopes across the cell was expected to occur upon further cycling. The anode was not completely replaced by ⁶Li since the neutron absorption for that isotope is so much higher that all detail would be obscured as very few neutrons would be transmitted through to the detector. One reason that this type of setup has not been investigated previously using neutrons, despite the attractiveness of the isotope selectivity offered by lithium, has been the insufficient resolution available from existing neutron imaging instruments. However, with the development of a high-resolution setup that allows pixel sizes down to 1.5 μm, detail can now be resolved down to length scales of 4 μm.^[41,42]

2. Results and Discussion

While in situ neutron tomography can facilitate 3D representation of the lithium distribution through a cell at specific states of charge, 2D radiography, conducted operando, can visualize dynamic changes in lithium concentration during lithiation and delithiation. Here, the cell was cycled in the neutron beam while radiography was performed, recording the neutron transmission every 6 s. Additionally, 3D tomographies were measured at selected states of charge that included the fully charged and discharged cell. Initial processing of the radiography data accounted for the background subtraction, while two normalization methods were performed. The true neutron transmission was attained by using the flat field, or empty beam, measurements while normalization relative to the initial pristine state enabled the change in the number of transmitted neutrons relative to the initial state to be visualized. However, since these images are a 2D projection of a cylindrical cell, the path taken by the neutrons through the sample is not constant across the image. This can be resolved by using the Beer–Lambert law (Equation 1), where Σ , is dependent on both the beam transmission, defined as the ratio, I/I_0 ,

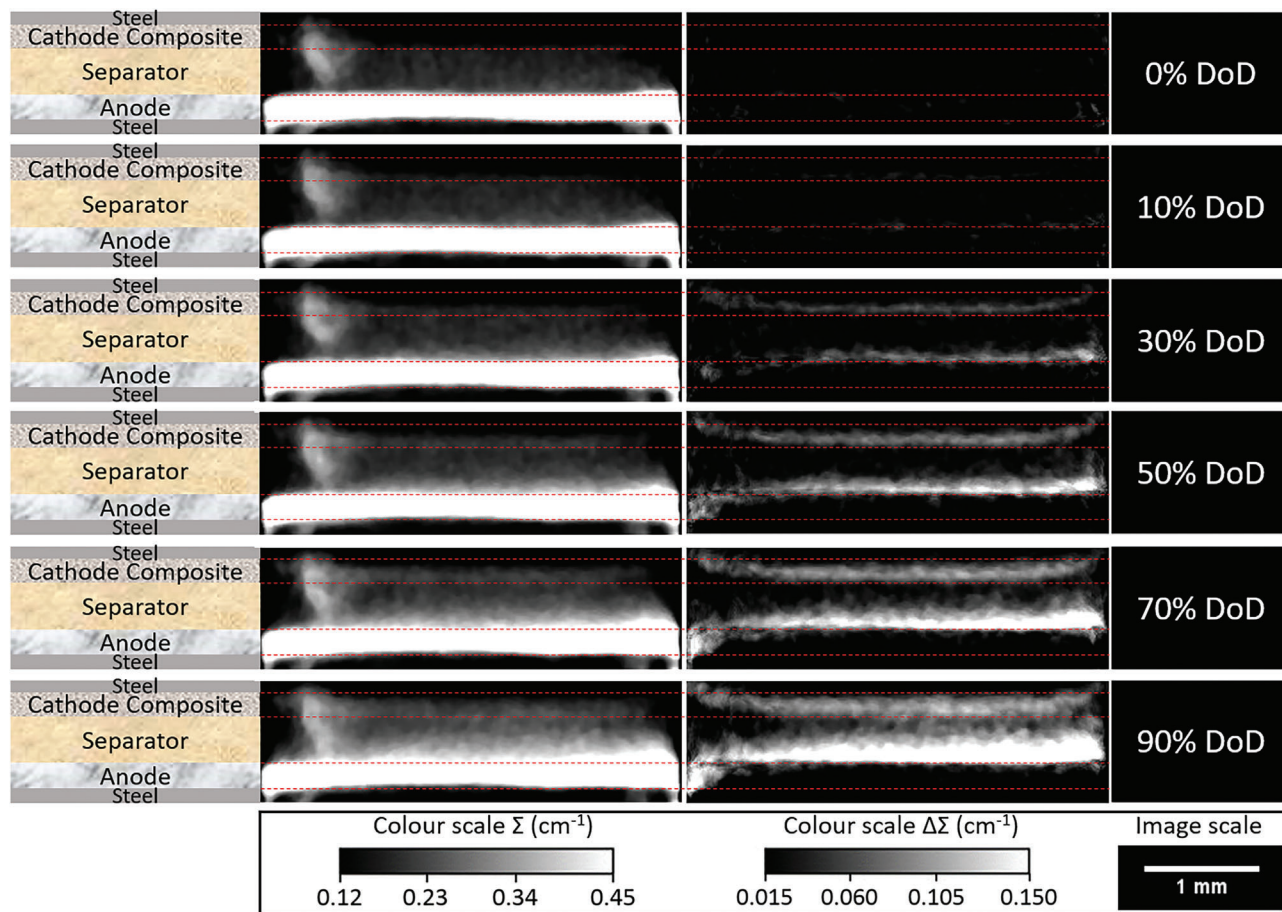


Figure 2. Series of radiography images of the cell showing how the neutron attenuation changes with the degree of discharge (DoD), that is, lithium progression from anode to cathode. The images on the left are normalized to the background and represent the neutron attenuation, Σ , while those on the right are normalized to the initial state and illustrate where the greatest changes in the attenuation, $\Delta\Sigma$, occur.

between the transmitted beam intensity, I , and the incident beam intensity, I_0 , and the neutron path length through the sample, l_p .

$$\Sigma = -\frac{1}{l_p} \ln \frac{I}{I_0} \quad (1)$$

After calculation of l_p for each pixel individually, depending on the normalization method, the absolute or change in attenuation for each pixel in each image across the duration of the operando measurement can be displayed as a 2D matrix representation of each component of the cell, as a function of time. Since the cell volume is essentially fixed between the two steel current collectors, the change in attenuation for each cell component as a function of time could be determined.

Lithium, with the exception of the immobile In in the anode, absorbs neutrons to a significantly greater extent than the other elements contained in the cell. Thus, as the Li is transported through the cell, the pattern of attenuation changes. In an all ^{nat}Li -containing cell, where all Li is of the same isotopic mixture and therefore has the same neutron attenuation coefficient, it would not be possible to distinguish the Li^+ ions from the anode diffusing through the electrolyte from the Li^+ ions that were originally in the $\text{Li}_6\text{PS}_5\text{Cl}$ separator. It would also not be possible

to determine conclusively any information about the origin of the Li in the Li_2S formed in the cathode. However, this is not the case for the cell featured here, as is evident in **Figure 2**, where Σ , and the change in attenuation, ($\Delta\Sigma$), are displayed at regular intervals during the initial discharge. In the case of the absolute neutron attenuation (left) there is an observed lightening across the separator region corresponding to an increase in attenuation during discharge. This is even more evident when only the change of attenuation (right) is considered. Here, the diffusion front through the separator region from the anode to the cathode is clear and the progression with the degree of discharge, (DoD), is notable. The increased attenuation in the cathode resulting from the accumulation of lithium in the form of Li_2S is also observed. This latter behavior is also visible in a cell containing lithium with only the naturally occurring isotope mixture since there has been an overall change in the amount of lithium in this region.^[39] However, in this earlier cell, the separator region did not exhibit any visible changes in the neutron images since there was negligible net change in the amount of lithium present in this region (see Supporting Information). These image series clearly show the advantage of varying the isotopic mixtures of one or more cell components. Furthermore, by considering the cross-section of the cell and taking the median attenuation for a

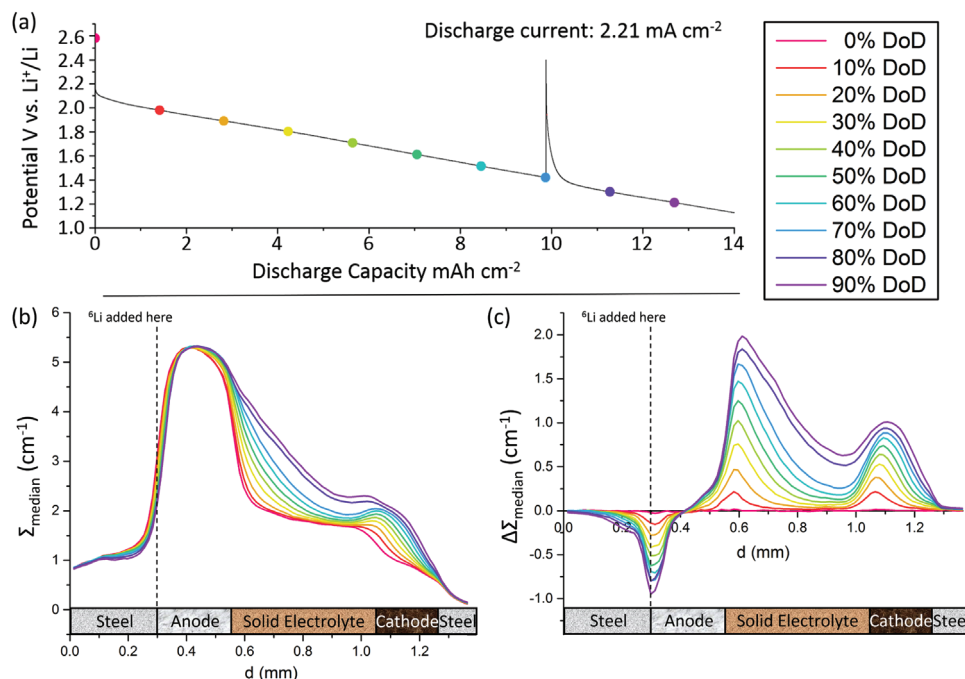


Figure 3. a) Voltage decrease of the investigated cell, displayed as a function of discharge capacity, for the initial discharge. Each highlighted data point represents the degree of discharge, DoD, in 10% intervals. The peak at around 10 mAh cm^{-2} corresponds to the voltage relaxation from when an in situ tomography was performed. b,c) Plots displaying median neutron attenuation, (Σ_{median} , (b)) and change in neutron attenuation, ($\Delta\Sigma_{\text{median}}$, (c)) as a function of d for the 10% intervals of the initial discharge highlighted in (a). The component interfaces are shown below each plot as a guide for the eye. The vertical dashed line denotes where the additional ^6Li was located during cell assembly.

given position in the vertical plane of the cell (d , mm), a clearer picture of the changes to each component of the cell can be visualized (Figure 3). Data are shown for 10% intervals in DoD during the initial discharge (Figure 3a). For both series, Σ and $\Delta\Sigma$, the separator and cathode all display distinct attenuation changes across their depth as the cell is discharged. In the case of the anode, the changes are subtle and only readily discernible for the $\Delta\Sigma$ plots (Figure 3c). The attenuation in the main part of the anode remains unchanged while there is a decrease on the side nearest the current collector—anode interface. This is accompanied by a corresponding increase on the side with the anode—separator interface. This can be described as a shift in $^6\text{Li}^+$ ion concentration from the area adjacent to the current collector, where the ^6Li was added during cell assembly, in the direction of the Li^+ ion flow as the cell is discharged.

Although the ^6Li is much more highly neutron absorbing than any other component, its relative amount compared to the indium, the next most absorbing element, is small. Thus, at the current collector—anode interface, the effect on Σ (Figure 3b) is small since the absorption from the indium is unchanged and still the dominant contribution. However, if we consider $\Delta\Sigma$ (Figure 3c) then the only changes are due to lithium ion transport and the reduction of the ^6Li proportion in this localized region as the cell is discharged is observable. In the separator region the effect is even more pronounced as what can be described as a front of ^6Li enriched Li^+ ions proceeds through the solid electrolyte. However, as is especially evident from Figure 3c, this front does not appear to have fully reached the separator—cathode composite interface until the cell has been discharged

to a significant degree. Nevertheless, as Figure 3b shows, the cathode displays an immediate increase in attenuation, initially at the side of the separator—cathode interface, then spreading deeper into the cathode, resulting from an increased lithium presence in the form of Li_2S . As can be seen in Figure 2, the rate of diffusion of lithium through the separator is not uniform but taking the median attenuation for a given d allows a clearer demonstration of the front progression. This observation of Li_2S formation immediately upon the commencement of discharge, preceding the point at which lithium ions from the anode reach the cathode composite, demonstrates the ability of neutron radiography to initially differentiate the two sources of contrast present—the ^6Li enriched Li diffusing through the electrolyte separator and the net increase in Li content in the cathode.

Once the front of ^6Li enriched lithium ions reaches the cathode, this ability to differentiate between them is no longer possible. Thus, 2D radiography measurements have the most utility during the initial discharge of the cell where the capability of neutron radiography for operando measurements provides information on the dynamics of diffusion as a function of DoD. The limitations from the 2D nature of neutron radiography means that discussion of lithium progression can only be made in terms of d . The use of 3D neutron tomography is required to view the homo- or hetero-geneous distribution of lithium for a given d . The nature of the technique requires measurement in situ since it involves the acquisition of a series of images as the cell is rotated, which can then be subsequently reconstructed into a 3D representation of the sample. As such, a series of tomographies were recorded for the fully charged or discharged

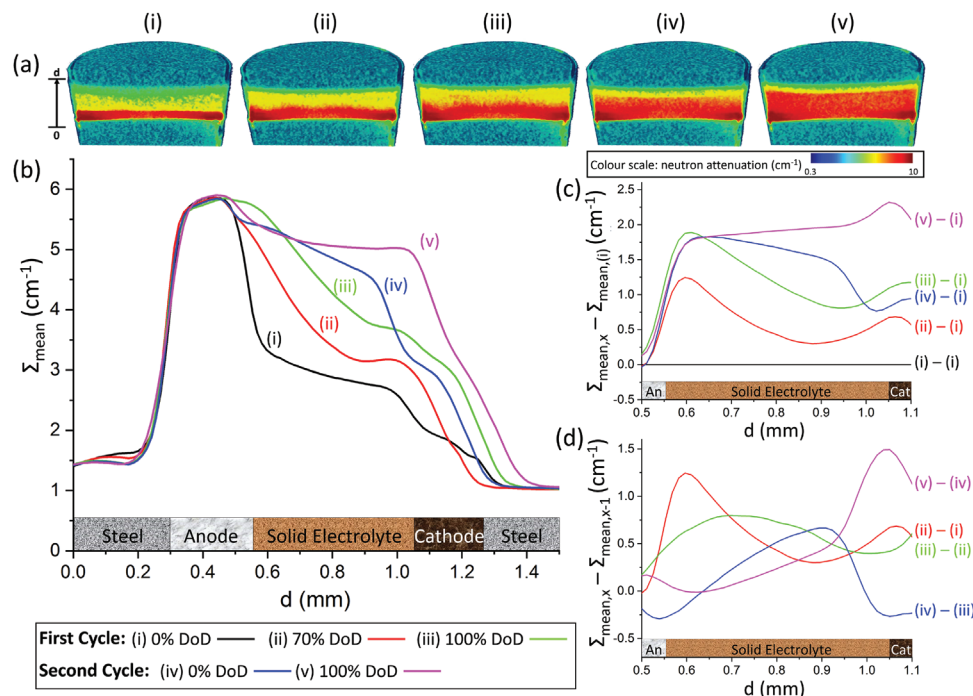


Figure 4. a) 3D tomographies for each DoD (i–v) showing the ^6Li progression through the cell. Each tomography has been sectioned vertically for clarity. The blue at the top and bottom represents the end of the steel current collectors while the deep red at the bottom of tomography (i) clearly shows the position of the anode. The arrow shows the range of d displayed in b–d) while the color bar displays the attenuation range. b) Plot showing how the mean neutron attenuation (Σ_{mean}) changes across the cell at various DoD over two cycles (cycle 1: (i–iii), cycle 2: (iv–v)) from 3D tomography measurements. c) Plot showing how the solid electrolyte separator for each dataset in (b) changes with respect to the pristine state (i). d) Plot showing how the solid electrolyte separator for each dataset in (b), ‘tomography x ’, where x is from (ii) to (v), changes with respect to the previous measured state, ‘tomography $x-1$ ’.

cell over two cycles, with an additional measurement for a partially discharged cell during the initial discharge (Figure 4a). It should be noted that the tomography data will be affected by the beam hardening effect which disproportionately affects highly attenuating elements such as In and ^6Li . Here, the effect was observed to be severe in the anode which contains both ^6Li and In but reduced elsewhere. A beam hardening correction was considered but not applied to permit quantitative comparison of the different tomographies since the procedure radially changes the values of attenuation. 3D reconstructions of the tomography (Figure 4a) demonstrate the capabilities of neutron imaging in directly visualizing the lithium ion transport through the solid electrolyte. The anode is shown at the bottom in red while the blue that sandwiches the cell represents the steel current collectors. The yellow/green denotes the solid electrolyte separator and cathode composite. Changes in the solid electrolyte separator are caused by the changes to the lithium isotope ratio while in the cathode it is primarily the increased lithium mass (as Li_2S) with an additional contribution from variation in the isotope ratio. While the ^6Li progression through the solid electrolyte is distinct in each image in Figure 4a, using these measurements to calculate the mean attenuation as a function of d , in a similar way to the radiography analysis in Figure 3, shows with greater nuance the ^6Li progress through the solid electrolyte separator toward the cathode. These changes can be more readily discerned in combination with Figures 4c,d which show, respectively, the attenuation changes relative to the pristine state tomography

(i) and those relative to the previous measured tomography, that is, (iii) relative to (ii) etc. As expected, tomographies related to the initial discharge of the cell, pristine, (i, black), partially discharged, (ii, red) and fully discharged, (iii, green), show clearly the attenuation increase across the SE separator associated with the ^6Li diffusion in both Figures 4b,c. However, it is only in Figure 4d that the ^6Li diffusion front, exhibited here as the greatest change in attenuation (peak maximum), becomes discernible. In the partially discharged state, (ii–i, red), this peak is adjacent to the anode–separator interface but has proceeded to the centre of the separator after full discharge, (iii–ii, green). The broadening of the peak from (ii–i) to (iii–ii) is most likely reflective of the increasing distance from the source of ^6Li ions in the anode. Returning to Figure 4b, it is notable after the first full discharge (iii, green) that, while the isotopic ratio between the ^6Li and ^7Li in the $\text{Li}_6\text{PS}_5\text{Cl}$ has changed in favor of increased ^6Li , it has not yet reached an equilibrium point with the ratio of the Li isotopes in the ^6Li enriched anode, even accounting for the In in the anode. However, by the second cycle discharged state (v, magenta) the noticeable plateau of attenuation across the depth of the separator layer in Figure 4b suggests that parts of the separator are approaching an equilibrium distribution, though Figure 4d suggests there are still changes from (iv) to (v) focused on the cathode side of the separator. It can also be seen in Figure 4b that after charging (iv, blue) the attenuation is only reduced below that of the fully discharged state (iii, green) for d values that are in close proximity to the anode–separator

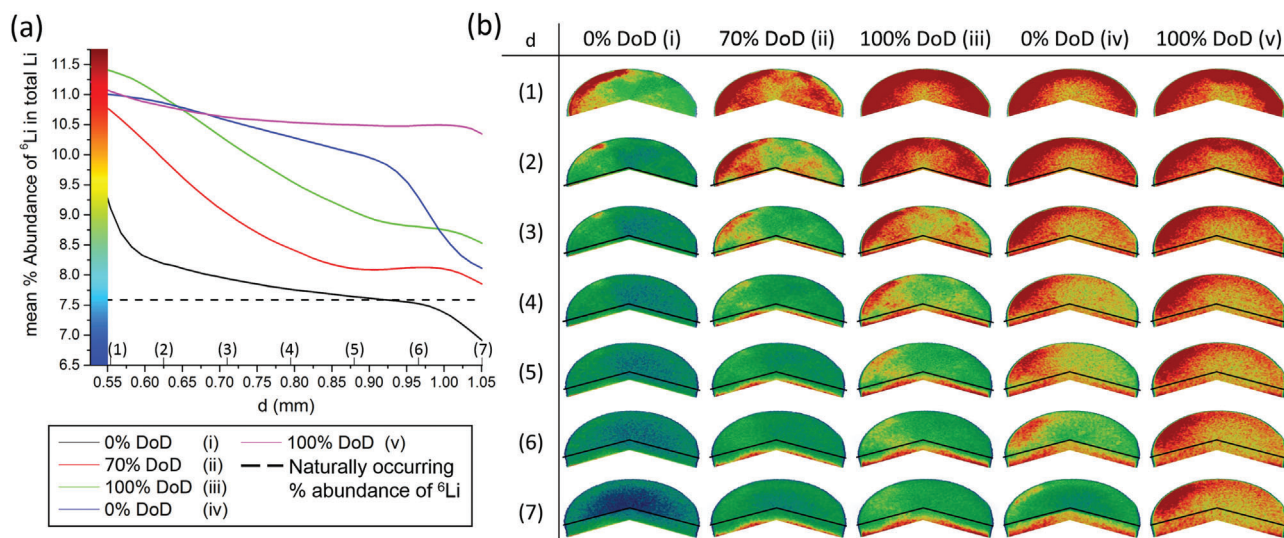


Figure 5. a) Plot showing the mean percentage abundance of the ${}^6\text{Li}$ isotope in the lithium contained within the solid electrolyte separator region. Data is calculated using the tomographies recorded at the labeled charge state (i–v). The color scale pertains to the images shown in (b). b) 3D representations showing the inhomogeneity of the percentage abundance of the ${}^6\text{Li}$ isotope, for each of the charge states shown in (a), at regular intervals through the solid electrolyte separator (1–7). Each row shows the full depth of the electrolyte separator at that d starting from the anode—separator interface at the bottom of the image to the current d position at the top with the black line marking the edge of vertical/horizontal plane.

and separator—cathode interfaces. This feature is not clear in Figure 4c since it is obscured by the large overall changes relative to the initial state. However, it is evident in the blue plot in Figure 4d, displaying the change when going from the discharged state (iii) to recharged state (iv), which shows a dip below zero near the anode—separator interface. This is followed by a steady increase reflecting the deepening ${}^6\text{Li}$ penetration to higher d observed in Figure 4b. The region around the anode—separator interface shows the highest Σ_{mean} in the entire separator region due to the immediate proximity to the source of the ${}^6\text{Li}$ enriched lithium so a reversal of the applied current will force lithium ions from a less ${}^6\text{Li}$ saturated area toward the interface thus lowering the net attenuation. A similar situation is found at the separator—cathode interface which is responsible for an even greater attenuation reduction, and consequent dip below zero, between the discharged and recharged state (iv–iii, blue) in Figure 4d since here the source of lithium ions during charging is the cathode composite where the ${}^6\text{Li}/{}^7\text{Li}$ ratio is much lower than elsewhere in the cell at this point. In the central part of the separator there is an overall increase in Σ_{mean} (Figure 4b) for each measurement from the pristine through to the final second discharged state. In addition to the current induced ${}^6\text{Li}$ transport through the separator there is ${}^6\text{Li}$ diffusion even without an applied current due to localized ${}^6\text{Li}$ - ${}^7\text{Li}$ concentration gradients. This explains the continued Σ_{mean} increase from the discharged (green) to the recharged state (blue) in both Figure 4b (from iii to iv) and Figure 4c (from iii–i to iv–i) despite the applied current having been reversed during the intervening period of operando radiography. This is most clearly observed in the centre of the separator, away from the interfaces with the anode and cathode with their aforementioned external influence on the Li distribution in the separator. A gradient across the SE separator in the pristine state (i, black) can be observed in Figure 4b. This is likely due to a combination of a rough interface between the anode and

solid electrolyte, at low d , and localized diffusion of lithium ions prior to measurement, now noticeable due to the lithium isotope manipulation in the anode (observed to a lesser degree in the separator region of the all ${}^{\text{nat}}\text{Li}$ containing cell in Figure 1c).

The discussion to this point has focused on the changes to the neutron attenuation and the inhomogeneous nature of these changes in the solid electrolyte separator. These effects are observable with neutron imaging due to changes in the lithium isotope ratio resulting from enriching the anode with ${}^6\text{Li}$ and thus modifying the naturally occurring isotope mixture. As such, we have attempted to quantify the percentage abundance of ${}^6\text{Li}$ in the solid electrolyte using the assumption that initially the $\text{Li}_6\text{PS}_5\text{Cl}$ solid electrolyte contains Li with the naturally occurring mix and has a neutron attenuation coefficient of 2.755 cm^{-1} , calculated for 2.8 \AA neutrons as described in Table 1.

Ideally, it would be possible to use the pristine tomography data in this calculation but, as has been noted earlier, there already exists a gradient across the depth of the separator preventing use of this method. The results of this calculation are shown in Figure 5, showing only the solid electrolyte region since there are Li mass changes in addition to the isotope ratio variation in the anode and cathode. A continuous view of the mean percentage abundance across the depth of the solid electrolyte separator region is displayed in (a). A direct visualization of the inhomogeneous ${}^6\text{Li}$ progression through the separator, at several intervals in d , from the anode/SE interface adjacent to image series (1) to the SE/cathode interface adjacent to image series (7) is shown in (b) for each tomography, (i–v). Here, the deviation from a homogeneous electrolyte for the pristine state (i) is clear with the ${}^6\text{Li}$ already visible around the edge in image (i,1) in Figure 5b. This does not arise from a tilt in the cell as registration of all tomographies after reconstruction accounted for this possibility.

Two main trends can be identified here that are also visible in the mean attenuation values shown in Figure 4b. First, as

d increases, that is, proceeding away from the ${}^6\text{Li}$ enriched anode, the percentage abundance of ${}^6\text{Li}$ drops, which is consistent across the slice area, irrespective of the charge state of the cell. The ${}^6\text{Li}$ enriched anode has a ${}^6\text{Li}/{}^7\text{Li}$ ratio that initially is greater than that of the lithium contained in the solid electrolyte. As the cell is discharged this ratio in the electrolyte changes in favor of the Li isotope ratio in the anode. When it has undergone sufficient charge/discharge cycles, it is to be expected that the Li isotope ratio in the separator region will be similar to that of the anode. It will not have directly comparable attenuation due to the presence of other elements—those with low attenuation in the $\text{Li}_6\text{PS}_5\text{Cl}$ electrolyte and the highly attenuating indium in the anode. However, the rate at which this isotopic ratio changes will be greater at lower d due to the shorter diffusion distance from the source of the ${}^6\text{Li}^+$ ions in the anode, as noted in the discussion of Figure 4d and something also observed in the operando radiography measurements during the initial discharge in Figure 3b. Therefore, there will be a negative attenuation gradient, and thus ${}^6\text{Li}$ abundance gradient, with increasing d , as calculated in Figure 5a and directly observed in each vertical image series in Figure 5b. The images in the first column of Figure 5b show a generally low ${}^6\text{Li}$ abundance (green - blue) with a small patch of higher attenuation/ ${}^6\text{Li}$ abundance (red) at the edge in the first image most likely sufficient to elevate the mean value that is observed in Figure 5a at low d . Second, as the cell is progressively cycled the penetration of the ${}^6\text{Li}$ extends deeper into the solid electrolyte. Therefore, at low d , the rate of increase in ${}^6\text{Li}$ abundance decreases, as observed in the flattening of the gradients in Figure 5a from (i) to (v). Although the ${}^6\text{Li}$ proportion continues to increase, demonstrated by the increasing saturation of high attenuation/ ${}^6\text{Li}$ abundance values as you proceed along each row in Figure 5b, these changes have a lesser overall effect on the mean percentage abundance for a slice at a given d . Looking at the images in more detail, it is interesting to note that at low d the mean percentage ${}^6\text{Li}$ abundance is higher for the discharged state in the first cycle (iii) than it is in the second cycle (iv and v). Looking at the images in rows (1) and (2) we can see that, while there is a high saturation of ${}^6\text{Li}$ around the periphery of the cell, the central areas display a fluctuation in the degree of red versus orange/yellow between images in column (iii) and those in columns (iv and v). It might be argued that a ring of high attenuation (represented here as a high percentage abundance of ${}^6\text{Li}$) is a feature of beam hardening, a commonly experienced issue. However, the asymmetry of the highest saturation values around the edge of the cell that has a cylindrical geometry suggest that this is a real effect and not an artefact of the neutron imaging process. This can especially be observed in column (v) but also in the deep red areas of images in the other columns. Beam hardening is, nevertheless, a phenomenon that needs to be considered when dealing with a highly neutron attenuating element such as ${}^6\text{Li}$. Another notable feature in Figure 5a is the decrease in percentage abundance of ${}^6\text{Li}$ at position (7) for the recharged state, (iv), below that of the discharged state, (iii). The close proximity to the cathode is no doubt the cause of this decrease with Li-ions from the cathode with a lower ${}^6\text{Li}$ abundance entering the SE separator during charging. This effect is difficult to discern clearly when comparing images (iii,7) and (iv,7) in Figure 5b though there is a general trend of yellow to green and green to blue when switching between particular regions of images (iii,7)

and (iv,7). This decrease in ${}^6\text{Li}$ abundance over much of the image area is sufficient to offset the increase in ${}^6\text{Li}$ abundance in a small region at the left hand edge of image (7,iv) that is also evident when comparing rows (3–7) of tomographies (iii) and (iv). Additionally, the fully discharged cell from the second cycle (v) appears in Figure 5a to have reached a state of quasi-saturation with the mean percentage abundance barely changing at higher d suggesting a consistent distribution of ${}^6\text{Li}$ across the separator. This is interesting since at high d the ${}^6\text{Li}$ enriched lithium ions from the anode will have had to travel the furthest from their source and yet it already appears that there is no longer a d dependent gradient of their distribution. However looking at the images for this discharged state in Figure 5b in comparison with the charged state (columns v and iv, respectively) shows that while the distribution may be consistent with d , especially for images (v,3–7) it is not homogeneous which suggests that the second discharge results in an increase in the ${}^6\text{Li}$ abundance across the depth and breadth of the solid electrolyte separator but that the packing density in some areas of the $\text{Li}_6\text{PS}_5\text{Cl}$ is more conducive to lithium ion transport than others. The ionic conductivity dependence on stack and fabrication pressure in sulfide based solid electrolytes has already been observed.^[43] The use of a ${}^6\text{Li}$ enriched anode has permitted these preferential pathways, that are formed during the fabrication process, to be visualized for the first time.

3. Conclusion

In the present study, we have demonstrated the utility of the radically different neutron absorption properties of the two predominantly occurring isotopes of lithium when used in conjunction with operando neutron radiography and in situ neutron tomography to visualize lithium ion transport during cycling of a solid-state Li–S battery. By enrichment of the Li–In anode of an all solid-state Li–S battery with highly neutron absorbing ${}^6\text{Li}$ we have shown that it is possible to visualize the diffusion of lithium ions from the anode through the solid electrolyte separator under electrochemical operation. This is information not previously accessible when measurements were made with a similar cell that did not vary the lithium isotopic ratio.^[39]

2D radiography, concentrating on the initial discharge when attenuation changes compared to the pristine state are most clear, demonstrated dynamically the attenuation changes across the cell, with the caveat that changes in the anode and cathode are a combination of changes in amount of lithium as well as lithium isotope ratio. Normalization with the background showed how the absolute attenuation changes across the cell while normalization to the initial state elucidated where in the cell the greatest changes occur. The latter demonstrates that in the separator region there is a consistent increase in the ${}^6\text{Li}$ proportion with degree of discharge, most strongly in the vicinity of the anode, but extending out further in the cell in the form of a reaction front. 3D tomography visualized the degree of homogeneity of the lithium percolation through the separator region highlighting the changing ${}^6\text{Li}$ distribution between the discharged and charged states. This work makes an important initial step in the characterization of lithium ion transport through solid electrolyte separators combining neutron imaging with selective lithium isotope enrichment. The potential is clear for future study in the dynamics

of lithium ion transport through solid electrolytes with the aim of identifying transport pathways an important next step.

4. Experimental Section

Materials and Cell Preparation: For this study, an all-solid-state battery, comprising a Li–In anode, $\text{Li}_6\text{PS}_5\text{Cl}$ solid electrolyte separator and a C/S/ $\text{Li}_6\text{PS}_5\text{Cl}$ cathode, was selected to be the model system. A custom-built aluminium casing was used as the cell housing (Figure 1a) due to the low absorption of neutrons by aluminium, with the cylindrical geometry optimal for operando measurements. The contents of the battery were protected from moisture and air with O-ring seals while electrical insulation was attained through use of a polyimide sheath (Kapton, inner diameter 4.06 mm, wall thickness 70 μm , Goodfellow) between the cell stack and the casing. Continuous contact between the components was maintained through use of two stainless steel stamps that doubled as current collectors. All cell components were dried prior to assembly for 24 h at 60 °C under dynamic vacuum (< 1 mbar). These were tightened with a torque of 4 Nm, corresponding to approximately 60 MPa of internal pressure. A 200 μm thick cathode, delivering an areal capacity of almost 12 mAh cm^{-2} and a 560 μm thick solid electrolyte layer were used to optimize visualization of changes to the cell under operation. A total of 13 mg of the solid electrolyte, $\text{Li}_6\text{PS}_5\text{Cl}$ and 5 mg of the composite cathode were used in the preparation. During this process all materials were handled under an argon atmosphere ($p(\text{O}_2)/p < 1$ ppm, $p(\text{H}_2\text{O})/p < 5$ ppm). The solid electrolyte $\text{Li}_6\text{PS}_5\text{Cl}$ was synthesized via a solid-state reaction. Lithium sulfide (Li_2S , Sigma–Aldrich, 99.98 %), phosphorus pentasulfide (P_2S_5 , Sigma–Aldrich, 99%) and anhydrous lithium chloride (LiCl, Alfa Aesar, 99%) were mixed in a stoichiometric ratio and ground for 15 min in an agate mortar. The resulting powder was manually pelletized and sealed into evacuated, carbon-coated quartz ampoules that had been pre-heated to 1073 K to remove residual moisture. These samples were subsequently annealed at 823 K for 7 days (ramp 100 K h^{-1}). After grinding the pellets, phase purity was checked via X-ray diffraction (XRD) using a PANalytical Empyrean powder diffractometer with Bragg–Brentano θ – θ geometry and a Cu $K\alpha$ X-ray source. Conductivity measurements were performed on isostatically pressed 10 mm diameter pellets containing approximately 200 mg of electrolyte. For contact, ion blocking gold electrodes were deposited via thermal evaporation on both sides. Conductivities were calculated based on the geometric dimensions of the sample. The conductivity of $\text{Li}_6\text{PS}_5\text{Cl}$ was determined to be 1.8 mS cm^{-1} . The C/S/ $\text{Li}_6\text{PS}_5\text{Cl}$ mixture was prepared with a 1:2:3 weight ratio via ball milling. Carbon black ECP600J (LION) was used as a conductive additive. In the case of the anode, a 200 μm thick indium foil (4 mm diameter, ChemPur 99.999%) and a 120 μm thick lithium foil (diameter 2 mm, Sigma–Aldrich 99.9%) were pressed onto the separator. The lithium in the foil was comprised of the naturally occurring ratio of the ^6Li and ^7Li isotopes. In addition, 0.2 mg of pure ^6Li (Sigma–Aldrich 96%) was added to the anode to enrich the ^6Li content before the current collector was attached. Characterization of the cell composition, using a number of techniques including electrochemical impedance spectroscopy (EIS), X-ray photoelectron spectroscopy (XPS) and scanning electron microscopy (SEM), was done prior to the neutron imaging measurements.^[18,44,45]

Neutron Imaging: Neutron imaging has been used here to visualize changes to the spatial distribution of the lithium throughout the cell upon cycling through quantification of the changing neutron attenuation along the cell axis. The enrichment of the ^6Li content in the anode in the pristine state, in contrast to the naturally occurring mixture of ^7Li and ^6Li elsewhere in the cell, only serves to enhance these changes to the Li distribution in the separator and cathode regions under operation, while not changing the cell chemistry. The data presented here were measured using the NeXT (Neutron and X-ray Tomography) instrument at the Institut Laue–Langevin (ILL), Grenoble, France. It is capable of recording both 2D radiography images as well as 3D tomographies, where a series of angular projections are recorded and subsequently combined to create a 3D representation of the cell. Here, radiography measurements were performed

operando while the cell was being cycled and at predetermined potentials the cycling was paused while an in situ tomography was recorded. Each measurement used white beam neutrons with wavelengths between 2 and 6 Å, with a maximum intensity at around 2.8 Å. The sample position was located 10 m from a 3 cm pinhole for an L/D = 333. The cell was attached to a height-adjustable rotation stage to permit 360° tomographies to be recorded. Images were recorded using a Hamamatsu ORCA 4V2 sCMOS camera in combination with a 20 μm thick aluminium coated Gadox ($\text{Gd}_2\text{O}_2\text{S}$) scintillator. The attached camera lens had a focal length of 50 mm (Canon), which, in conjunction with infinity corrected optics^[46] employing an objective lens that had a focal length of 55 mm (Heliflex), yielded an adjusted pixel size of 14.2 μm , after 2 x 2 binning, and a field of view of 14.54 mm x 14.54 mm. During the tomography measurements, the sample was rotated through 360° while 1216 projections were taken. The camera continuously recorded images throughout the experiment, each with an exposure time of 2 s and with three frames medianised per projection. Additionally, dark field measurements were made, with the beam off, in conjunction with a series of flat field, empty beam, measurements.

The tomography data were reconstructed using the Octopus software^[47] a dedicated tomography image reconstruction program while visualization in 3D of the reconstructed tomographies was done using the Volume Graphics software.^[48] All radiography data were reconstructed using the ImageJ image processing program.^[49]

The linear neutron attenuation coefficients for the various elements that comprised the cell, along with aluminium that formed the casing, are shown in Table 1. The values were calculated using the NIST Activation and Scattering Calculator^[50] for neutrons at a wavelength of 2.8 Å, which corresponds to the maximum in the spectral distribution for a polychromatic neutron beam on the NeXT instrument.^[41]

Cell Cycling Behavior: Galvanostatic cycling was performed using a Biologic potentiostat (BCS-815) between 0.5 and 2.5 V vs. In/InLi (which corresponds to 1.12 V and 3.12 V vs. Li^+/Li) with a current density of 2.21 mA cm^{-2} and a discharge rate of 0.1 C. The measured cell showed an open circuit potential of 2.58 V vs. Li^+/Li which was consistent with previous results.^[18] The cycling performance of the cell is displayed in Figure 3a which highlights the initial discharge and the DoD utilized in the radiography analysis while the full two-cycle electrochemistry profile is shown in the Supporting Information.

Supporting Information

Supporting Information is available from the Wiley Online Library or from the author.

Acknowledgements

This research was supported by the German Federal Ministry of Education and Research (BMBF) within the project LISZUBA under grant numbers 03XP0115A and 03XP0115C. The authors acknowledge the invaluable work of Ms. Boyana Kozhuharova in the registration of the 3D tomography data. The authors acknowledge the assistance of the NI-Matters program at the ILL during the acquisition of the data. The authors confirm that there are no conflicts of interest.

Open access funding enabled and organized by Projekt DEAL.

Author Contributions

I.M. and W.G.Z. designed the study. R.B. designed the operando cell. G.F.D. synthesized materials, prepared the cathode composites, and assembled the cells. R.B., G.F.D., A.T., L.H., and N.K. performed the imaging measurements. R.B. and N.K. analyzed the data. R.B. interpreted the data. R.B. prepared the initial draft of the work. All authors gave comments and edited the manuscript.

Conflict Of Interest

The authors declare no conflict of interest.

Data Availability Statement

Research data are not shared.

Keywords

6-lithium, lithium–sulfur, lithium isotope, neutron imaging, neutron tomography, neutron radiography, solid-state

Received: March 7, 2023

Revised: April 24, 2023

Published online: June 6, 2023

- [1] B. Dunn, H. Kamath, J.-M. Tarascon, *Science* **2011**, 334, 928.
- [2] C. Capasso, O. Veneri, *Appl. Energy* **2014**, 136, 921.
- [3] N. Nitta, F. Wu, J. T. Lee, G. Yushin, *Mater. Today* **2015**, 18, 252.
- [4] D. Larcher, J.-M. Tarascon, *Nat. Chem.* **2015**, 7, 19.
- [5] J. Janek, W. G. Zeier, *Nat. Energy* **2016**, 1, 16141.
- [6] W. Chen, J. Liang, Z. Yang, G. Li, *Energy Procedia* **2019**, 158, 4363.
- [7] A. A. Kebede, T. Kalogiannis, J. Van Mierlo, M. Berecibar, *Renewable Sustainable Energy Rev.* **2022**, 159, 112213.
- [8] P. G. Bruce, S. A. Freunberger, L. J. Hardwick, J.-M. Tarascon, *Nat. Mater.* **2012**, 11, 19.
- [9] A. Manthiram, X. Yu, S. Wang, *Nat. Rev. Mater.* **2017**, 2, 16103.
- [10] S. Randau, D. A. Weber, O. Kötz, R. Koerver, P. Braun, A. Weber, E. Ivers-Tiffée, T. Adermann, J. Kulisch, W. G. Zeier, F. H. Richter, J. Janek, *Nat. Energy* **2020**, 5, 259.
- [11] S. Wang, M. Tang, Q. Zhang, B. Li, S. Ohno, F. Walther, R. Pan, X. Xu, C. Xin, W. Zhang, L. Li, Y. Shen, F. H. Richter, J. Janek, C.-W. Nan, *Adv. Energy Mater.* **2021**, 11, 2101370.
- [12] Y. Lee, J. Jeong, H. J. Lee, M. Kim, D. Han, H. Kim, J. M. Yuk, K.-W. Nam, K. Y. Chung, H.-G. Jung, S. Yu, *ACS Energy Lett.* **2022**, 7, 171.
- [13] H.-J. Peng, J.-Q. Huang, Q. Zhang, *Chem. Soc. Rev.* **2017**, 46, 5237.
- [14] S. Dörfler, H. Althues, P. Härtel, T. Abendroth, B. Schumm, S. Kaskel, *Joule* **2020**, 4, 539.
- [15] Q. Pang, L. F. Nazar, *ACS Nano* **2016**, 10, 4111.
- [16] X. Yang, J. Luo, X. Sun, *Chem. Soc. Rev.* **2020**, 49, 2140.
- [17] K. Zhu, C. Wang, Z. Chi, F. Ke, Y. Yang, A. Wang, W. Wang, L. Miao, *Front. Energy Res.* **2019**, 7, 123.
- [18] S. Ohno, C. Rosenbach, G. F. Dewald, J. Janek, W. G. Zeier, *Adv. Funct. Mater.* **2021**, 31, 2010620.
- [19] C. Yu, S. Ganapathy, E. R. H. v. Eck, H. Wang, S. Basak, Z. Li, M. Wagemaker, *Nat. Commun.* **2017**, 8, 1086.
- [20] N. Boaretto, I. Garbayo, S. Valiyaveetil-SobhanRaj, A. Quintela, C. Li, M. Casas-Cabanas, F. Aguesse, *J. Power Sources* **2021**, 502, 229919.
- [21] A. Sakuda, A. Hayashi, M. Tatsumisago, *Chem. Mater.* **2010**, 22, 949.
- [22] K. H. Kim, Y. Iriyama, K. Yamamoto, S. Kumazaki, T. Asaka, K. Tanabe, C. A. J. Fisher, T. Hirayama, R. Murugan, Z. Ogumi, *J. Power Sources* **2011**, 196, 764.
- [23] T. Gustafsson, J. O. Thomas, R. Koksang, G. C. Farrington, *Electrochim. Acta* **1992**, 37, 1639.
- [24] O. Pecher, J. Carretero-González, K. J. Griffith, C. P. Grey, *Chem. Mater.* **2017**, 29, 213.
- [25] X. Wei, X. Wang, X. Tan, Q. An, L. Mai, *Adv. Funct. Mater.* **2018**, 28, 1804458.
- [26] L. Sang, R. T. Haasch, A. A. Gewirth, R. G. Nuzzo, *Chem. Mater.* **2017**, 29, 3029.
- [27] Z. Liu, J. Scott Cronin, Y. K. Chen-Wiegart, J. R. Wilson, K. J. Yakal-Kremski, J. Wang, K. T. Faber, S. A. Barnett, *J. Power Sources* **2013**, 227, 267.
- [28] S. Müller, J. Eller, M. Ebner, C. Burns, J. Dahn, V. Wood, *J. Electrochem. Soc.* **2018**, 165, A339.
- [29] X. Lu, A. Bertei, D. P. Finegan, C. Tan, S. R. Daemi, J. S. Weaving, K. B. O'Regan, T. M. M. Heenan, G. Hinds, E. Kendrick, D. J. L. Brett, P. R. Shearing, *Nat. Commun.* **2020**, 11, 2079.
- [30] S. Chattopadhyay, A. L. Lipson, H. J. Karmel, J. D. Emery, T. T. Fister, P. A. Fenter, M. C. Hersam, M. J. Bedzyk, *Chem. Mater.* **2012**, 24, 3038.
- [31] S. Bessette, A. Paoletta, C. Kim, W. Zhu, P. Hovington, R. Gauvin, K. Zaghbi, *Sci. Rep.* **2018**, 8, 17575.
- [32] J. B. Siegel, X. Lin, A. G. Stefanopoulou, D. S. Hussey, D. L. Jacobson, D. Gorsich, *J. Electrochem. Soc.* **2011**, 158, A523.
- [33] J. B. Siegel, A. G. Stefanopoulou, P. Hagans, Y. Ding, D. Gorsich, *J. Electrochem. Soc.* **2013**, 160, A1031.
- [34] H. Zhou, K. An, S. Allu, S. Pannala, J. Li, H. Z. Bilheux, S. K. Marthia, J. Nanda, *ACS Energy Lett.* **2016**, 1, 981.
- [35] M. Lanz, E. Lehmann, R. Imhof, I. Exnar, P. Novák, *J. Power Sources* **2001**, 101, 177.
- [36] R. F. Ziesche, J. B. Robinson, M. D. R. Kok, H. Markötter, W. Kockelmann, N. Kardjilov, I. Manke, D. J. L. Brett, P. R. Shearing, *J. Electrochem. Soc.* **2020**, 167, 130545.
- [37] R. F. Ziesche, J. B. Robinson, H. Markötter, R. Bradbury, A. Tengattini, N. Lenoir, L. Helfen, W. Kockelmann, N. Kardjilov, I. Manke, D. J. L. Brett, P. R. Shearing, *J. Electrochem. Soc.* **2020**, 167, 140509.
- [38] R. F. Ziesche, T. Arlt, D. P. Finegan, T. M. M. Heenan, A. Tengattini, D. Baum, N. Kardjilov, H. Markötter, I. Manke, W. Kockelmann, D. J. L. Brett, P. R. Shearing, *Nat. Commun.* **2020**, 11, 777.
- [39] R. Bradbury, G. F. Dewald, M. A. Kraft, T. Arlt, N. Kardjilov, J. Janek, I. Manke, W. G. Zeier, S. Ohno, *Adv. Energy Mater.* **2023**, 13, 2203426.
- [40] L. Magnier, L. Lecarme, F. Alloin, E. Maire, A. King, R. Bouchet, A. Tengattini, D. Devaux, *Front. Energy Res.* **2021**, 9, 657712.
- [41] A. Tengattini, N. Lenoir, E. Andó, B. Giroud, D. Atkins, J. Beaucour, G. Viggiani, *Nucl. Instrum. Methods Phys. Res., Sect. A* **2020**, 968, 163939.
- [42] A. Tengattini, N. Kardjilov, L. Helfen, P.-A. Douissard, N. Lenoir, H. Markötter, A. Hilger, T. Arlt, M. Paulisch, T. Turek, I. Manke, *Opt. Express* **2022**, 30, 14461.
- [43] M. Cronau, M. Szabo, C. König, T. B. Wassermann, B. Røling, *ACS Energy Lett.* **2021**, 6, 3072.
- [44] S. Ohno, R. Koerver, G. Dewald, C. Rosenbach, P. Tischer, D. Steckermeier, A. Kwade, J. Janek, W. G. Zeier, *Chem. Mater.* **2019**, 31, 2930.
- [45] G. F. Dewald, S. Ohno, J. G. C. Hering, J. Janek, W. G. Zeier, *Batteries Supercaps* **2021**, 4, 183.
- [46] S. H. Williams, A. Hilger, N. Kardjilov, I. Manke, M. Strobl, P. A. Douissard, T. Martin, H. Riesemeier, J. Banhart, *J. Instrum.* **2012**, 7, P02014.
- [47] <https://octopusimaging.eu/>.
- [48] <https://volumegraphics.com/en/products/vgsm.html/>.
- [49] <https://imagej.net/>.
- [50] Neutron activation and scattering calculator, <https://www.ncnr.nist.gov/resources/activation/>.